



ROI Scissor: Interactive Segmentation of Feature Region of Interest in a Triangular Mesh

Ji-Hye Moon,¹ Yujin Ha,¹ Sanghun Park,² Myung-Soo Kim³ and Seung-Hyun Yoon¹

¹Department of Multimedia Engineering, Dongguk University, Jung-gu, South Korea
shyun@dongguk.edu

²Graduate School of Metaverse, Sogang University, Mapo-gu, South Korea

³Department of Computer Science and Engineering, Seoul National University, Gwanak-gu, South Korea

Abstract

We present a simple and effective method for the interactive segmentation of feature regions in a triangular mesh. From the user-specified radius and click position, the candidate region that contains the desired feature region is defined as geodesic disc on a triangle mesh. A concavity-aware harmonic field is then computed on the candidate region using the appropriate boundary constraints. An initial isoline is chosen by evaluating the uniformly sampled ones on the harmonic field based on the gradient magnitude. A set of feature points on the initial isoline is selected and the anisotropic geodesics passing through them are then determined as the final segmentation boundary, which is smooth and locally shortest. The experimental results show several segmentation results for various 3D models, revealing the effectiveness of the proposed method.

Keywords: anisotropic geodesic, geometry processing, harmonic field, interaction, mesh segmentation, user interface design

CCS Concepts: • Computing methodologies → Computer graphics; Shape analysis

1. Introduction

Mesh segmentation plays an important role in shape matching, parameterization, texturing and remeshing in geometric modelling and processing. Existing methods are either based on automatic or interactive algorithms, depending on the level of user intervention. Even if automatic methods [AZC*11, LLZ*15, XLZ18, ZLS*20] produce plausible segmentation results, sophisticated applications require many user interventions for semantic segmentation.

Recently, harmonic fields have been widely used in both automatic and interactive mesh segmentation [ZT10, AZC*11, MFL11, ZTA11, ZLL*15, LLZ*15, LDB17]. Au *et al.* [AZC*11] presented an automatic mesh-segmentation method based on a set of concavity-aware harmonic fields with large variations across concave regions. The harmonic fields are computed by solving a Laplacian system derived from a concavity-sensitive weighting scheme, and then the segmentation boundaries are determined as isolines with the maximum gradient magnitude. Zheng *et al.* [ZTA11] proposed a novel single-click interface, called the *dot scissor*, for interactive mesh segmentation. This method requires only a single mouse

click to specify the proximity location through which the desired segmentation boundary passes. From the user's click position, four concavity-aware harmonic fields are generated, and the uniformly sampled isolines are voted on for selecting the optimal isoline. This interface is effective and easy to use; however, the user is restricted to only clicking on the concave boundary region. Therefore, for example, if the user intends to segment the right tooth in Figure 1a by clicking on the middle concave region of two teeth, the left tooth may be segmented.

The minima rule suggested by Hoffman *et al.* [HR84, HS97] described that based on human perception, people tended to cut a shape along concave regions in the direction of the minimum principal curvature. Segmentation methods based on the harmonic field employ concavity information as a key measure for the underlying algorithm, and the resulting segmentation boundaries generally satisfy the minima rule. However, people tend to segment shapes along the shortest boundary locally, which is not guaranteed by the isoline sampled from the harmonic field. Therefore, post-processing is required to shorten the segmentation boundary [JLCW06].

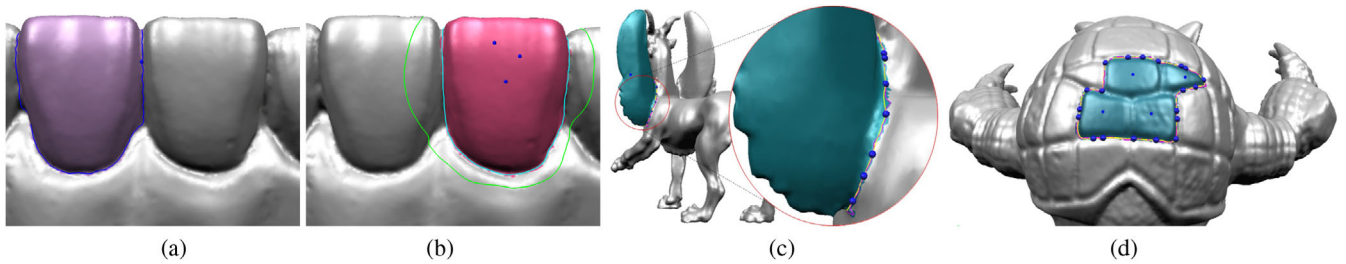


Figure 1: Effectiveness of the proposed method: (a) undesired segmentation from a click on the middle region of the teeth; (b) consistent segmentations from arbitrary points in the ROI; (c) smooth and locally shortest segmentation boundary in yellow and (d) additive segmentation using multiple mouse clicks.

To efficiently compute the locally shortest segmentation boundary, Zhuang *et al.* [ZZCJ14] proposed an interactive mesh-segmentation technique. They defined live wires as geodesics in a new tensor-based anisotropic metric and introduced an effective mesh-embedding approach to efficiently compute anisotropic geodesics. Their method generated the locally shortest segmentation boundary that was aligned with the features and curvature directions. However, their method required many user interventions to specify the intermediate points through which the geodesics would pass.

In this paper, we present a simple and effective method for interactive mesh segmentation that combines the strengths of the harmonic field [AZC*11, ZTA11] and anisotropic geodesics [ZZCJ14]. A candidate region that contains the feature region of interest (ROI) is defined as geodesic disc which can be specified by a single mouse click for centre position followed by mouse scroll for radius. A segmentation harmonic field sharply varying over the boundary of an ROI is then generated and an initial segmentation boundary is chosen from the uniformly sampled isolines on the harmonic field. Some feature points on the initial segmentation boundary are selected, and then, the anisotropic geodesics passing through them are determined as the final segmentation boundary. In our method, unlike that in Refs. [ZTA11, ZZCJ14], mouse clicks are not restricted to concave regions and user interventions are not required to construct the anisotropic geodesics. Therefore, consistent segmentation boundaries can be obtained through a single mouse click on an arbitrary point in the feature region as long as the candidate region contains that region.

Figure 1 shows the representative results of the proposed method. Our method allows the user to click on an arbitrary point in the feature ROI while producing consistent segmentation results. For example, even though the user clicks three different points (in blue) on the right tooth in Figure 1b, consistent segmentation results are obtained as long as the right tooth is inside the candidate region (in green). Additionally, the segmentation boundary is represented by an anisotropic geodesic, which is smooth and locally shortest, compared with the isolines selected from the concavity-aware harmonic field. Figure 1c shows the initial isoline (in magenta) and final segmentation boundary (in yellow). Furthermore, a feature region surrounded by a complex boundary can be easily segmented using the proposed method. Figure 1d shows the result of such a segmentation, which was obtained through four mouse clicks on different feature regions.

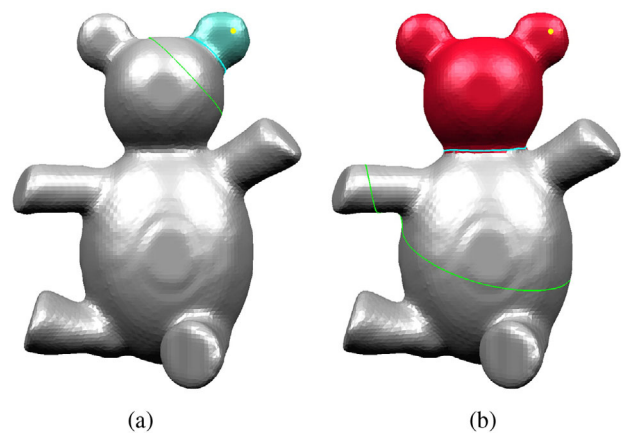


Figure 2: Different segmentation boundaries (in cyan) are generated depending on the candidate region (in green) even if the user clicks on the same point (in yellow) on the ear part in (a) and (b).

The proposed method in this paper has several advantages, which can be summarized as follows.

- To segment the desired feature region, the user simply needs to click on an arbitrary point in that region as long as the feature region is inside a candidate region (see Figure 1b).
- Our method provides an effective control mechanism for segmenting a specific feature region among several possible ones by allowing the user to control the radius of a candidate region at runtime (see Figure 2).
- The segmentation boundary generated in this paper is represented by anisotropic geodesics passing through feature points on the isoline selected from a concavity-aware harmonic field. Thus, it is smooth and locally shortest, compared to those generated by the existing methods (see Figure 1c).
- Boolean operations, such as the union or difference of geodesic discs, can define a new candidate region and thus, make it possible to segment the feature region of the complex boundary (see Figure 1d).
- The proposed method is insensitive to mesh resolution and geometric noise, while being able to produce stable and consistent segmentation results (see Figure 3).

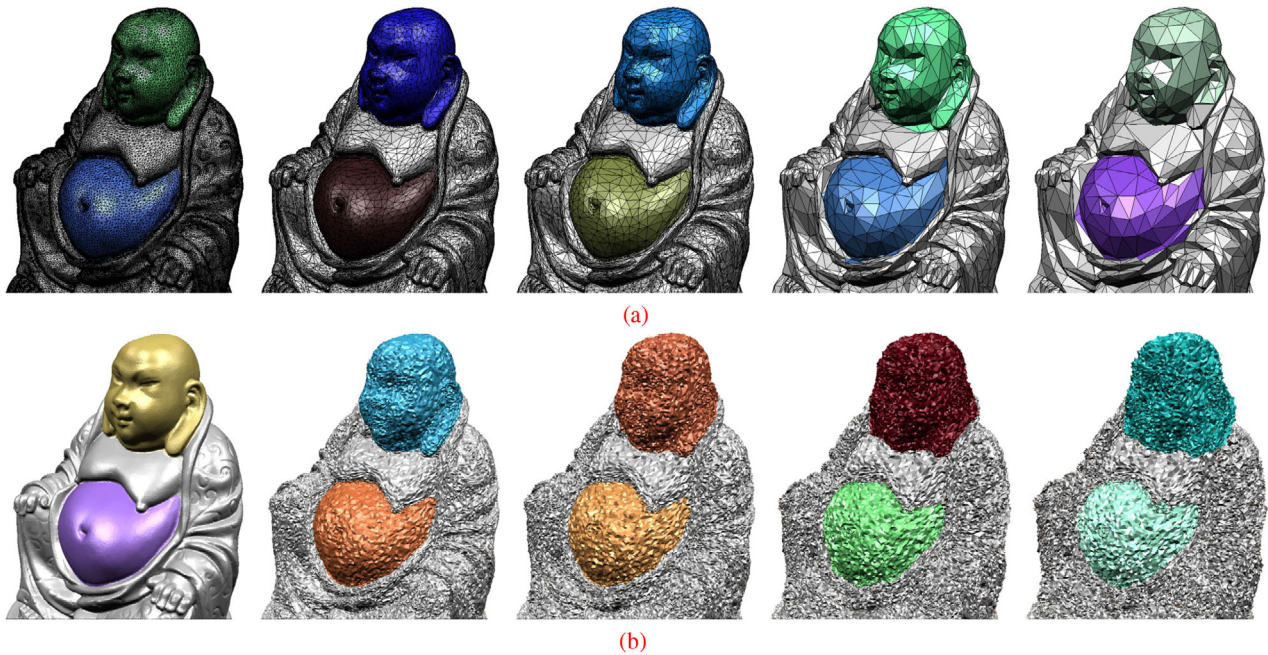


Figure 3: Insensitivity of proposed method to (a) mesh resolution and (b) geometric noise.

The remainder of this paper is organized as follows. In Section 2, we briefly review previous results on mesh segmentation. In Section 3, we improve the concavity-aware harmonic field and explain how to compute anisotropic geodesics on a triangular mesh, and in Section 4, we describe the proposed method. In Section 5, we present the experimental results and finally, in Section 6, we present the conclusion of the paper and suggestions for future work.

2. Related Work

In this section, we briefly review previous work on various mesh segmentation techniques that are directly related to our method. Automatic methods for mesh segmentation do not require user intervention, and numerous such techniques [AZC*11, LLZ*15, XLZ18, ZLS*20] have been proposed, ranging from purely geometric approaches to deep neural networks. In this paper, we restrict our discussion on previous work to interactive methods that require the minimum interaction of a user while providing semantically meaningful results. For a comprehensive review of mesh segmentation methods, we referred to a recent survey [RMG18].

Sophisticated methods with various types of user interactions have been proposed. Ji *et al.* [JLCW06] proposed a sketch-based method for interactive mesh segmentation. This method is based on a region-growing algorithm; it provides the users with an easy and effective way to mark strokes in the foreground and background while allowing them to select the ROI. Zheng *et al.* [ZT10] proposed two types of brushes: *part-brush* and *patch-brush*. The part-brush is used for constructing a harmonic field on semantic parts, and the patch-brush is used for flattening surface patches. Through these brushes, the user could select the desired region with a sin-

gle stroke. In this paper, we propose an interface similar to the dot scissor [ZTA11] for segmenting triangular meshes. However, our method does not restrict the user's click position to the concave region and provides consistent segmentation results even if the user clicks on arbitrary points in the desired region to be selected.

From a technical perspective, various algorithms have been employed for mesh segmentation, including region growing, watershed segmentation, clustering, and segmentation field. Region growing is a method of expanding the initial region while satisfying convexity, which was first inspired by the convex decomposition algorithm [CDST97]. Mangan and Whitaker [MW98, MW99] proposed a watershed method that was another type of 3D mesh segmentation based on image segmentation and analysis [Ser83]. Katz and Tal [KT03] proposed a new hierarchical mesh-decomposition algorithm based on fuzzy clustering and cuts. However, most of these methods did not guarantee that a closed segmentation boundary would be obtained. To resolve this limitation, segmentation methods [ZT10, ZTA11, AZC*11] based on a harmonic field have been proposed, wherein a closed segmentation boundary is determined as a closed isoline on the harmonic field.

In this paper, we employed a concavity-aware harmonic field with large variations across the concave regions. This approach has several advantages, such as being insensitive to mesh noise and changes in mesh posture. Concavity-aware harmonic fields have been widely used in various applications. Zou *et al.* [ZLL*15] applied it to the interactive tooth segmentation of dental meshes. Based on prior knowledge of human teeth, this method provides effective boundary constraints for constructing harmonic fields on dental meshes. Additionally, a refining strategy was introduced here to successfully segment teeth from a complicated dental mesh with indistinctive

tooth boundaries on the lingual surface. Later, this method was extended to the automatic segmentation of dental meshes [LLZ*15].

Generally, the isoline obtained from a harmonic field is neither smooth nor locally shortest. Thus additional post-processing is required to use it as the final segmentation boundary [JLCW06]. This is because the generated boundary tends to depend on the topology of the mesh rather than on the part to be segmented. Anisotropic geodesics can be effectively used for segmentation boundaries as an alternative to isoline. Zhuang *et al.* [ZZCJ14] defined a new tensor-based anisotropic metric to generate the shortest segmentation boundary along the feature and curvature directions. For computational efficiency, they proposed the mesh embedding approach and computed anisotropic geodesic efficiently using the existing geodesic algorithms [MMP87, SSK*05, CH90, XW09, CHK13]. In the *SeamCut* of Lucquin *et al.* [LDB17], isolines of harmonic fields are created with a few sketches, and the mesh is segmented by growing seams along anisotropic geodesic paths. Yang *et al.* [YWZK20] presented an intuitive user interface for dental mesh segmentation using the anisotropic geodesics proposed by Zhuang *et al.* [ZZCJ14].

In this paper, we employed two existing techniques; a concavity-aware harmonic field and anisotropic geodesics. However, we take a different approach to generating them. The concavity-aware harmonic field is generated by single mouse click on arbitrary points in ROI. For this, we propose new methods for computing edge weights and boundary constraints. The initial isoline selected from the harmonic field is not sufficient to serve as the desired segmentation boundary. To resolve this limitation, we present a method for computing anisotropic geodesics that align with the mesh features and curvature directions from the initial isoline.

3. Mathematical Background

This section introduces the fundamental techniques of the proposed method. Given a triangular mesh $M = (V, E)$, where V is the set of vertex indices and E is the set of edges, we present an effective way to construct a concavity-aware harmonic field with large variations across a concave region on M (Section 3.1) and compute anisotropic geodesic between two points that follows the geometric features of M (Section 3.2).

3.1. Concavity-aware harmonic field

Let $f : M \rightarrow R$ be a scalar function on a triangle mesh M and f_i be the corresponding function value of a vertex $i \in V$. The Laplace–Beltrami operator [MDSB03] (also known as Laplacian), when applied to f_i , produces the following expression:

$$\Delta f_i = \sum_{j \in N_1(i)} w_{ij}(f_j - f_i),$$

where $N_1(i)$ represents the one-ring neighbouring vertex indices of vertex i and w_{ij} is the weight of an edge $(i, j) \in E$. Intuitively, Δf_i is the sum of the weighted differences between f_j and f_i s, and the cotangent weight [MDSB03] is commonly used for various applications. The Laplacian of all the f_i s can be computed efficiently as

follows:

$$\Delta \mathbf{f} = \begin{bmatrix} \Delta f_1 \\ \Delta f_2 \\ \vdots \\ \Delta f_n \end{bmatrix} = L \begin{bmatrix} f_1 \\ f_2 \\ \vdots \\ f_n \end{bmatrix} = L\mathbf{f},$$

where n is the number of vertices and L is the $n \times n$ Laplacian (sparse) matrix that encodes the edge weights w_{ij} .

A harmonic field is a special type of scalar function of M that satisfies the Laplace equation $L\mathbf{f} = \mathbf{0}$ with Dirichlet boundary constraints. Let $\mathbf{f}_u = [f_1 \ \cdots \ f_m]^T$ be the unknown values for the unconstrained vertices and $\mathbf{f}_c = [f_{m+1} \ \cdots \ f_n]^T$ be the given values for the constrained vertices. Then the harmonic field can be constructed by solving the following linear system:

$$\begin{bmatrix} L_u & L_c \\ \mathbf{0} & I \end{bmatrix} \begin{bmatrix} \mathbf{f}_u \\ \mathbf{f}_c \end{bmatrix} = \begin{bmatrix} \mathbf{0} \\ \mathbf{f}_c \end{bmatrix} \Rightarrow L_u \mathbf{f}_u = -L_c \mathbf{f}_c, \quad (1)$$

where L_u and L_c are the submatrices of L and the unknown vector \mathbf{f}_u can be efficiently found by sparse Cholesky factorization [BKP*10].

Figure 4a shows an example of the harmonic field f which is constructed using two constraints: one (in red) and zero (in blue)—and cotangent weights; these weights are commonly used in various applications [MDSB03]. The uniformly sampled isolines (in white) show a smooth variation in f over the entire mesh M , which is suitable for shape deformation or approximation rather than mesh segmentation. To utilize a harmonic field for mesh segmentation, the field needs to have large variation in a concave region so that the uniformly sampled isolines are gathered at the concave region as densely as possible.

To produce such harmonic field, Au *et al.* [AZC*11] proposed a concavity-aware weighting scheme which defines edge weights as follows:

$$w_{ij} = \begin{cases} -\sum_{k \in N_1(i)} w_{ik} & \text{if } i = j, \\ \frac{|e_{ij}|}{G_{ij}} \beta & \text{if } (i, j) \in E, \\ 0 & \text{otherwise,} \end{cases} \quad (2)$$

where $|e_{ij}|$ is the length of the edge $(i, j) \in E$; and G_{ij} is the sum of the absolute Gaussian curvature at vertex i and j . In Equation (2), the constant β is a key component for generating large variation in a concave region. Au *et al.* [AZC*11] set $\beta = 0.01$ if either vertex i or j is concave, and $\beta = 1$, otherwise. Concave vertex can be identified by the following condition:

$$(\hat{\mathbf{p}}_i - \mathbf{p}_i) \cdot \mathbf{n}_i > 0, \quad (3)$$

where \mathbf{p}_i and \mathbf{n}_i are the position and normal of a vertex i and $\hat{\mathbf{p}}_i$ is the centroid of one-ring vertices. Figure 4b shows the harmonic field generated by this weighting scheme.

In this paper, we improve the weighting scheme in Equation (2) to produce a harmonic field with much larger variations in a concave region. The basic idea is to promote the step function β to a smooth function $\beta(\cdot)$ of mean curvature to better reflect the concavity. Concavity condition in Equation (3) only informs whether a

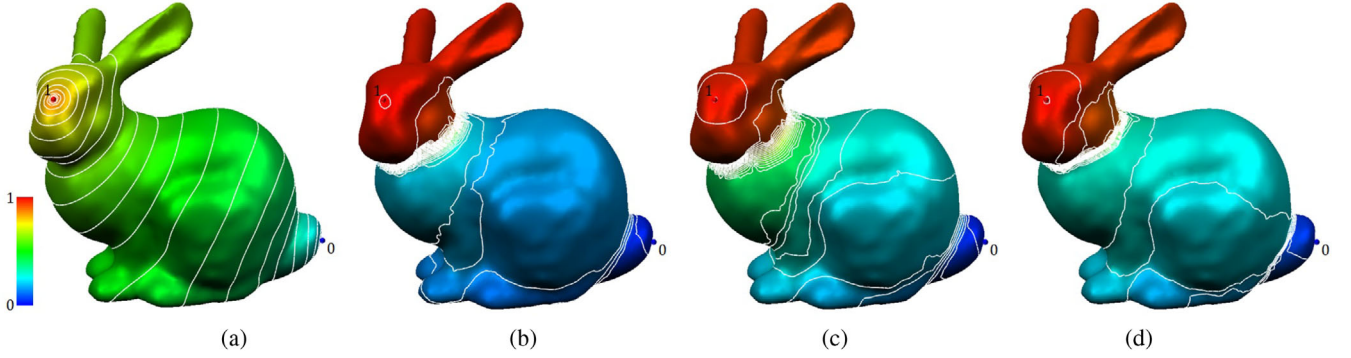


Figure 4: Comparison of harmonic fields generated by different weighting schemes: (a) cotangent weights; (b) concavity-aware weights in Au et al. [AZC*11]; (c) concavity-aware weights in Zheng et al. [ZTA11] and (d) weights under proposed method.

vertex is concave or not, but it does not give how much it is concave, which can be measured by mean curvature. Thus, we employ the mean curvature to sophisticate the concavity condition. Let \hat{H} be the maximum mean curvature and H_{ij} be the sum of the mean curvature at vertex i and j . We define $\beta(t)$ as follows:

$$\beta(t) = \begin{cases} \frac{1}{1+100t^2} & \text{if } t > 0, \\ 1 & \text{otherwise,} \end{cases}$$

where $0 \leq t (= \frac{H_{ij}}{2\hat{H}}) \leq 1$. Note that $\beta(t)$ is inversely proportional to H_{ij} and smoothly changes from 1 ($H_{ij} = 0$) to 0.01 ($H_{ij} = 2\hat{H}$), whereas a constant value $\beta = 0.01$ was used in Au et al. [AZC*11]. Figure 4d shows the harmonic field constructed using our weighting scheme, which exhibits much larger variations in concave regions. Note that more isolines are densely gathered at the neck and tail regions of the model compared to those in other weighting schemes in Figure 4b,c. Once a concavity-aware harmonic field is constructed, we choose the isoline with the highest score (see Section 4.2) and then improve it using an anisotropic geodesic (see Sections 3.2 and 4.3).

3.2. Anisotropic geodesics

Zhuang et al. [ZZCJ14] proposed an anisotropic distance metric such that the shortest geodesic followed the ridge, valley, and curvature directions. In this paper, we employed anisotropic geodesics [ZZCJ14] to improve the isoline selected from the concavity-aware harmonic field constructed by our weighting scheme.

Let $g_i(\mathbf{v})$ be a distance metric defined for each vertex $i \in V$ and a tangent vector \mathbf{v} at i . The length of vector \mathbf{v} is computed as follows:

$$g_i(\mathbf{v}) = \sqrt{\mathbf{v}^T M_i \mathbf{v}},$$

where M_i is a 2D symmetric tensor that controls the isotropy of the distance metric and is identical to the identity matrix for the Euclidean distance, M_i , which represents the anisotropic distance, can be determined as follows:

$$M_i = \begin{bmatrix} \mathbf{e}_1 & \mathbf{e}_2 \end{bmatrix} \begin{bmatrix} \lambda_1 & 0 \\ 0 & \lambda_2 \end{bmatrix} \begin{bmatrix} \mathbf{e}_1 & \mathbf{e}_2 \end{bmatrix}^{-1}, \quad (4)$$

where \mathbf{e}_i is the direction along which the vector length is modified by the value of λ_i . Several approaches [PSH*04, KMZ10, CBK12, ZZCJ14] exist for defining tensor-based anisotropic metrics. We employed the metric proposed by Zhuang et al. [ZZCJ14], who chose \mathbf{e}_1 (\mathbf{e}_2) as the direction of the maximum (minimum) normal curvature, and λ_1 and λ_2 as follows:

$$\lambda_1 = 1 + \gamma(|\kappa_1| - |\kappa_2|), \quad \lambda_2 = \frac{1}{\lambda_1}, \quad (5)$$

where κ_1 and κ_2 are the maximum and minimum normal curvatures, respectively, and $\gamma = 0.01$ is a user-specified constant. Consequently, the anisotropic metric determined using Equations (4) and (5) increases the length of a vector in the \mathbf{e}_1 direction and decreases it in the \mathbf{e}_2 direction because $\lambda_1 > 1$ and $\lambda_2 < 1$.

Based on the anisotropic metric discussed above, the edge length $|e_{ij}|$ can be modified such that it elongates (shortens) in the maximum (minimum) curvature direction. Figure 5 shows two geodesic distance fields computed by isotropic and anisotropic metrics, respectively, where the isolines (in grey) represent equidistance from the source vertex S . Note that the isolines are expanded along the minimum curvature direction and shrink along the maximum curvature direction. Moreover, the shortest geodesic path on the anisotropic metric follows the features and the minimum curvature direction; satisfying the minima rules of Hoffman et al. [HR84, HS97] for mesh segmentation based on human perception. Specifically, people tend to cut a shape along concave regions in the direction of the minimum principal curvature, as shown in Figure 5b. Additionally, it is not necessary to find an explicit triangular mesh with modified edge lengths because the geodesic distance field can be computed from edge lengths and connectivity, that is, the intrinsic representation of a triangular mesh. Further details on this can be found in Zhuang et al. [ZZCJ14].

The initial isoline selected from the concavity-aware harmonic field (Section 3.1) is neither smooth nor locally shortest. Therefore, it needs to be improved by anisotropic geodesics introduced in this section. Specifically, final segmentation boundary will be determined as anisotropic geodesics passing through key points sampled on the initial isoline (Section 4.3).

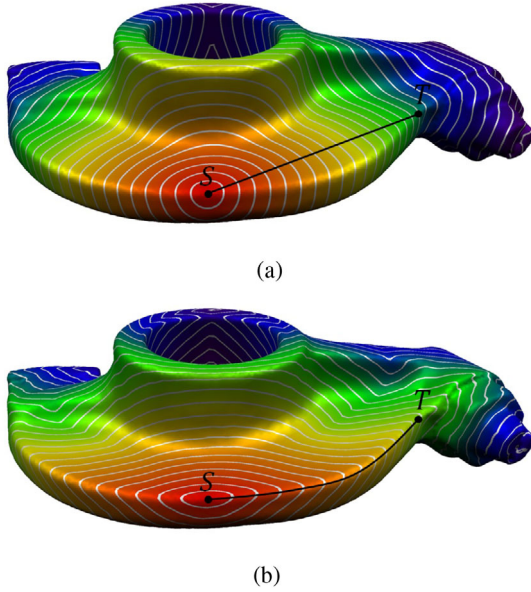


Figure 5: Shortest geodesic paths (in black) between S and T on (a) isotropic distance field and (b) anisotropic distance field.

4. ROI Scissor

By combining the concavity-aware harmonic field with anisotropic geodesics, we propose a simple and effective interface, called the *ROI scissor*, for interactively segmenting the feature ROI in a triangular mesh.

4.1. Boundary constraints

Boundary constraints play a crucial role in constructing a concavity-aware harmonic field and at least two boundary constraints are required to avoid the trivial solutions in Equation (1). Au *et al.* [AZC*11] located extreme vertices in a harmonic field constructed by a random vertex and used them as boundary constraints. Zheng *et al.* [ZTA11] sampled four pairs of points on a user-specified circle on a screen and projected them onto a triangular mesh to determine the boundary constraints of the harmonic field. Although this method provides an intuitive and easy-to-use interface, the user's input is limited to the concave region through which the segmentation boundary passes.

In this paper, we take a different approach to determining the boundary constraints. We also aim to compute the segmentation boundary of a feature region from a single mouse click, which can be an arbitrary point in the ROI. For this, a candidate region $C(r)$, which is a geodesic disc on a triangular mesh, is defined as follows:

$$C(r) = \{i \in V | d_g(i, s) < r\},$$

where r is the user-controllable radius and $d_g(i, s)$ is the geodesic distance to the vertex i from the source vertex s specified by the user's mouse click. The radius r can easily be controlled by mouse scroll at runtime and it remains unchanged until a new value is specified.

Once the candidate region has been determined, the appropriate boundary constraints are assigned to the vertices in $C(r)$. We assign one to the vertices whose geodesic distance to s is less than $0.1r$ and zero to the end vertices on the edges that intersected with the boundary of $C(r)$. The constant 0.1 for the constrained vertices of ones was determined empirically. For a smooth region, one vertex closest to the click position is sufficient, however, more vertices are necessary for bumpy region. Figure 6 shows the boundary (in green) of the candidate region and constrained vertices with ones (in red) and zeros (in blue), respectively.

Figure 7 shows two different harmonic fields constructed using the same source vertex s but different candidate regions. The candidate region in Figure 7a intersects with the ears of the Bunny model, while the one in Figure 7b covers entire head region. Consequently, different isolines (in white) are extracted depending on the user-specified radius r even if the same source vertex s is used. This provides a flexible mechanism for selecting the desired feature region by interactively controlling the size of the candidate region. For example, only the face region of the Bunny model is selected in Figure 8a, whereas the entire head part region is selected in Figure 8b.

Figure 9 shows two harmonic fields constructed using different sources in ROI but the same radius. The generated harmonic fields show large variation in the neck region similarly, which allows the user to click on arbitrary vertex in ROI to obtain similar segmentation results.

In most cases, the candidate region defined by one geodesic disc contains the ROI to be segmented. However, there are cases wherein the geodesic disc is not sufficient to cover feature regions with complex boundary shapes, as shown in Figure 10a. In this paper, we propose an efficient way to resolve this limitation by using Boolean operations, such as union and difference of geodesic discs. Figure 10b shows an example of the union of candidate regions defined by three mouse clicks and the corresponding harmonic field generated by the boundary constraints explained above. This mechanism significantly facilitates the user to interactively segment the desired region while adding or subtracting specific regions.

4.2. Initial segmentation boundary

Once the harmonic field is constructed from the user-specified vertex s and distance r , the next step is to choose an isoline that serves as the initial segmentation boundary. For this, we uniformly sample isolines I_i , where $i = 1, 2, \dots, m$. Let T be a triangle intersecting with I_i and f_j , where $j = 1, 2, 3$ be the harmonic value for each vertex of T . The gradient of the harmonic field on T is computed as follows [MDSB03]:

$$\nabla f_T = \frac{1}{2A_T} \sum_{j=1}^3 f_j \mathbf{e}_j^\perp,$$

where A_T is the area of triangle T and \perp denotes a counter-clockwise rotation of 90° in the triangle plane (see Figure 11). Note that the gradient ∇f_T is constant on triangle T and informs the direction along which the harmonic field varies maximally and $\|\nabla f_T\|$ indicates the amount of its variation. In this paper, we aim to choose an isoline \hat{l} across which the harmonic field exhibits the maximum

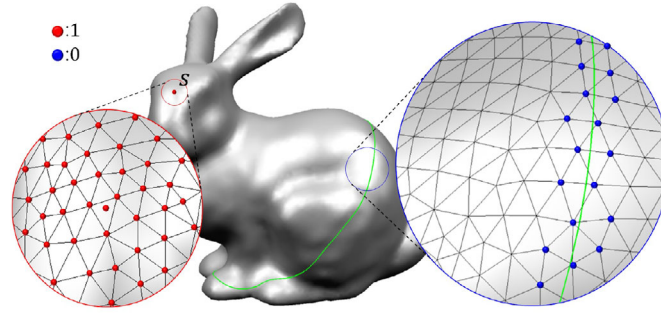


Figure 6: Candidate regions and the constrained vertices of one (in red) and zero (in blue).

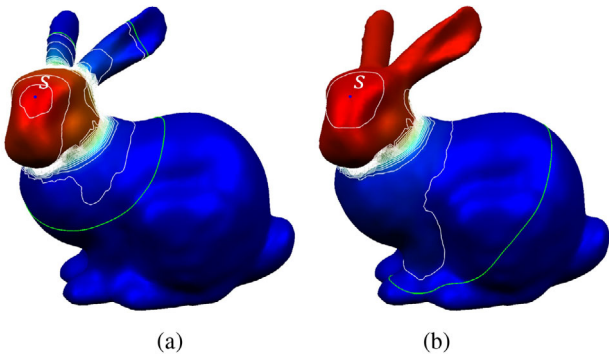


Figure 7: Generation of different harmonic fields in (a) and (b) by the same source vertex s depending on the radii of the candidate region.

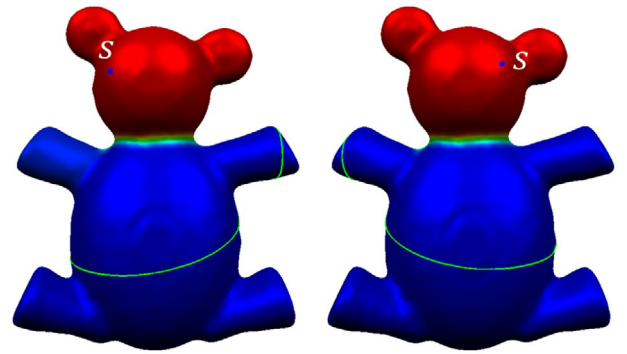


Figure 9: Generation of similar harmonic fields by two different source vertices in ROI.

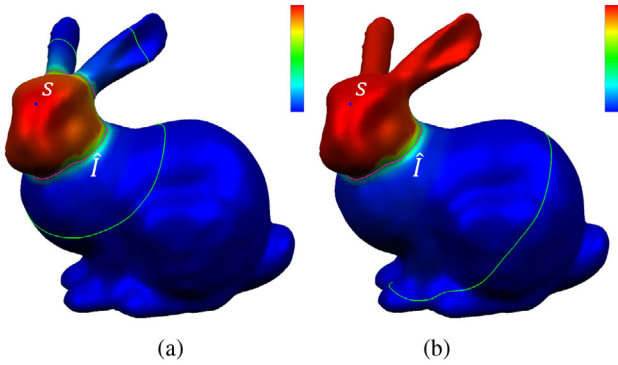


Figure 8: Different isolines \hat{I} (in magenta) are selected from the harmonic fields in Figure 7.

variation. For this purpose, we evaluate each isoline I_i by computing its score S_i as follows:

$$S_i = \sum_{T \in \hat{T}} \frac{|I_i \cap T|}{|I_i|} \|\nabla f_T\|,$$

where \hat{T} is the set of all the triangles intersecting with the isoline I_i ; and $|I_i|$ and $|I_i \cap T|$ are the lengths of I_i and the intersecting segment between I_i and T , respectively (see Figure 11). Isolines \hat{I} , which has

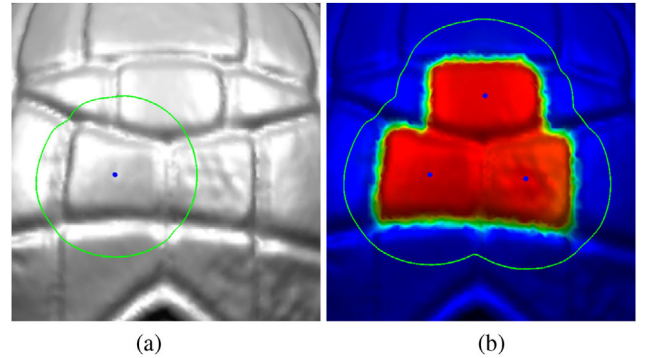


Figure 10: Concavity-aware harmonic field constructed by union of candidate regions.

the highest score, is then chosen for the initial segmentation boundary. Intuitively, S_i can be considered as the changing rate of a harmonic field per unit length of I_i .

Figure 8 shows two selected isolines \hat{I} (in magenta) with the highest scores among the uniformly sampled 50 isolines in Figure 7a,b, respectively. Note that the segmentation boundary may have two separate isolines with the same iso-value as shown in Figure 8a.

Our method can generate the segmentation field reliably, even if it is ambiguous to segment concave parts visually. The isolines

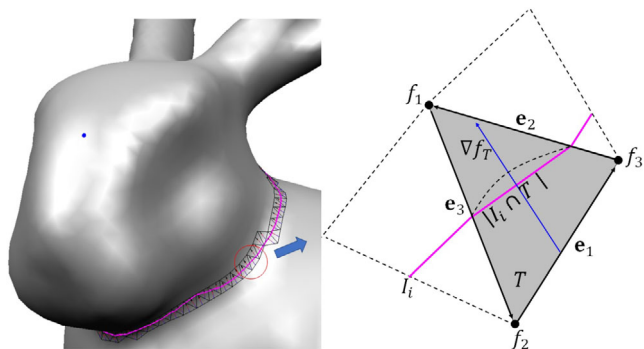


Figure 11: Computation of the score S_i of an isoline I_i (in magenta).

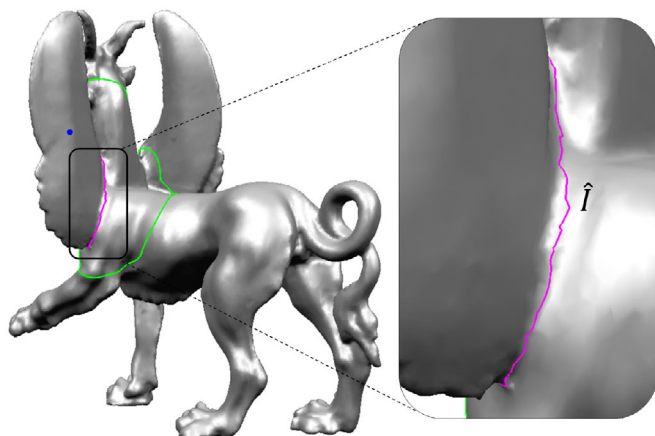


Figure 13: Initial isoline \hat{I} (in magenta) is neither smooth nor locally shortest.

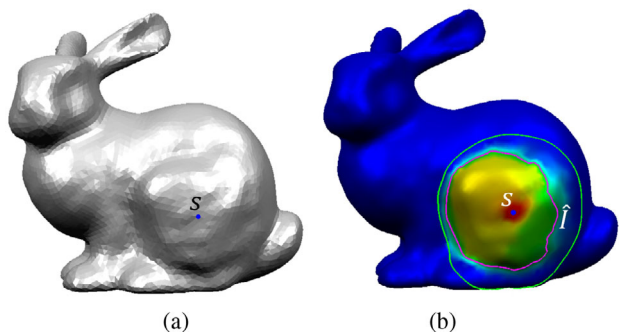


Figure 12: Initial isoline \hat{I} (in magenta) is selected robustly, even for the ambiguous concave region.

sampled from the segmentation field are always composed of a finite set of nonself-intersecting closed loops. For example, it is not easy to identify concave part on the lower right of the back leg the Bunny model in Figure 12a. However, our method can select the best isoline (in magenta) forming a round almost circular loop as shown in Figure 12b.

4.3. Geodesic segmentation boundary

Although the isoline \hat{I} , with the highest score, can be used for the final segmentation boundary of a feature region, \hat{I} is neither smooth nor locally shortest, as shown in Figure 13. This limitation can be resolved by employing the anisotropic geodesic introduced in Section 3. Specifically, we choose feature points $\mathbf{p}_1, \mathbf{p}_2, \dots, \mathbf{p}_k$ with a relatively higher mean curvature on \hat{I} and then find the closed anisotropic geodesic that passes through them.

To determine these feature points, we first divide the initial isoline \hat{I} into k segments with uniform length, that is, $\hat{I} = \hat{I}_1 \cup \hat{I}_2 \cup \dots \cup \hat{I}_k$. Let \hat{T}_i be the set of triangles intersecting with the i th segment \hat{I}_i . For each triangle in \hat{T}_i , we compute the mean curvature at its centroid and determine the centroid \mathbf{p}_i with the maximum curvature as the feature point \mathbf{p}_i in \hat{I}_i . In this manner, we can find the feature points (in blue), as shown in Figure 14a, where the model is visualized as a colour-coded mean curvature field. Finally, the geodesics

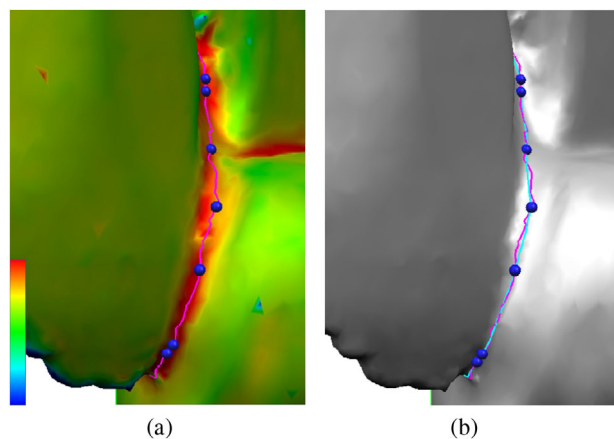


Figure 14: Computation of geodesic segmentation boundary: (a) feature point (in blue) with the highest mean curvature in each segment; and (b) resulting geodesic segmentation boundary (in cyan) passing through the feature points.

(in cyan) passing through the feature points is determined as the final segmentation boundary as shown in Figure 14b. We determined the number of segments as 10% of the number of triangles intersecting with the initial isoline \hat{I} , empirically. Figure 15 shows more examples of geodesic segmentation boundaries (in cyan) generated from the initial segmentation boundaries (in magenta) using the proposed method.

5. Experimental Results

The proposed method was implemented on a PC with an Intel Core i5-10400 processor, a 2.90-GHz CPU, 16 GB main memory and an NVIDIA GeForce GTX 1650 graphics card, using the C++ language. In this section, we demonstrate the effectiveness of the proposed method by segmenting the feature regions of various

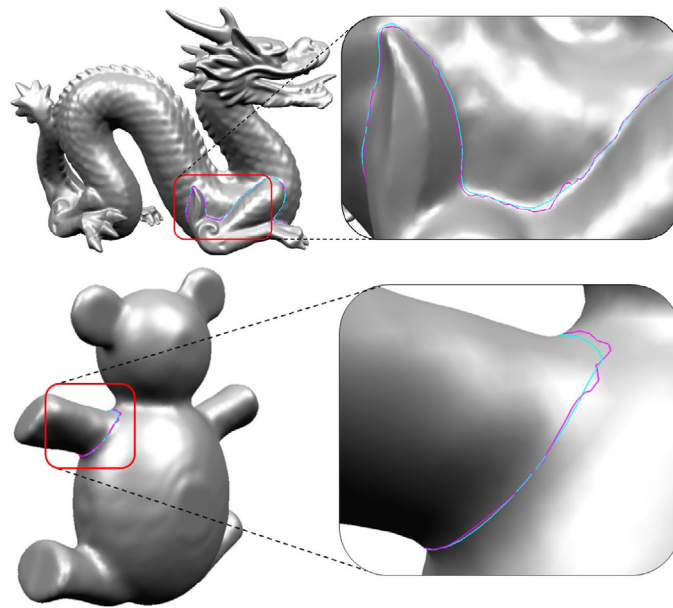


Figure 15: Geodesic segmentation boundaries (in cyan) generated from the initial isolines (in magenta).

triangular meshes that include the Princeton Segmentation Benchmark (PSB) dataset [CGF09] and 3D scanned tooth models.

5.1. Intuitive usability

Our primary goal is to provide the user with a mesh segmentation method that is easy-to-use and has intuitive usability. To segment the desired feature region, the user simply needs to click on an arbitrary point in the desired region. The geodesic segmentation boundary, which is smooth and locally shortest, gets automatically generated. To demonstrate the usability of the proposed method, various experiments were performed. Figure 16 shows the segmentation results of the three models used in the experiments. For each model, consistent segmentation boundaries (in cyan) were generated even though the user clicked three different points (in yellow) in the feature region. These examples demonstrate the usability of our method; that is, it produces similar segmentation results; as long as the user simply clicks on arbitrary points in the desired feature region. Compared with the dot scissor [ZTA11], our method provides the user with more flexibility in the click position; even users familiar with the dot scissor can easily use our method without difficulty.

5.2. Effective control and consistency

Our method provides an effective control mechanism for segmenting a desired feature region even when the user clicks on the same point. This mechanism can be easily realized by allowing the user to scroll the middle mouse button at runtime to control the radius of the candidate region. Figure 2 shows the controllability of our method; two segmentation results are compared, wherein the user clicks on the same point on the ear part; however, different segmentation results are obtained by the candidate regions (in green).

Combined with the Boolean operations of the candidate regions introduced in Section 4, this control mechanism significantly facilitates the segmentation of a feature region with a complicated boundary. For example, the user can add (remove) a feature region to (from) a previously segmented region while adjusting the radius of the candidate region. Figure 17 shows the union of the feature regions, where the final segmentation boundary is generated by four mouse clicks, and candidate regions of different radii are used for each segmentation. This type of additive segmentation would be challenging using existing methods [JLCW06, ZT10, ZTA11]. Figure 18a shows additional example of additive segmentation of 3D scanned tooth model, where a large candidate region (in green) is defined as the union of the geodesic discs specified by multiple clicks, and the teeth are segmented from the gums using appropriate boundary constraints. Figure 18b shows the results of individual tooth segmentation, as the user clicks on an arbitrary point on each tooth sequentially. Figure 18c,d shows the effects of the different sizes of candidate regions (in green) where too small candidate region may produce an undesired segmentation result (Figure 18c), which will be discussed in Conclusion.

The proposed method is insensitive to both geometric resolution and noise. Figure 3a shows the five segmentation results for the Buddha model with different numbers of triangles. Note that our method generated consistent segmentation boundaries despite the mesh resolutions being different. In addition, our method is insensitive to geometric noise and produces consistent segmentation results, as shown in Figure 3b.

5.3. Evaluation

Figure 19 shows three segmentation boundaries, each of which is generated by the dot scissor (in blue) [ZTA11], initial isoline

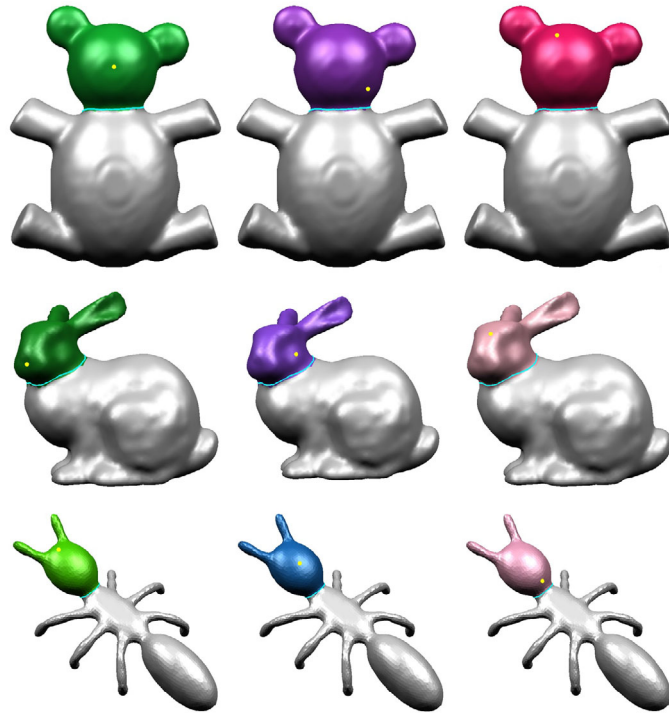


Figure 16: Segmentation results of three models; all segmentation boundaries (in cyan) for each model are generated from different user-clicked points (in yellow).

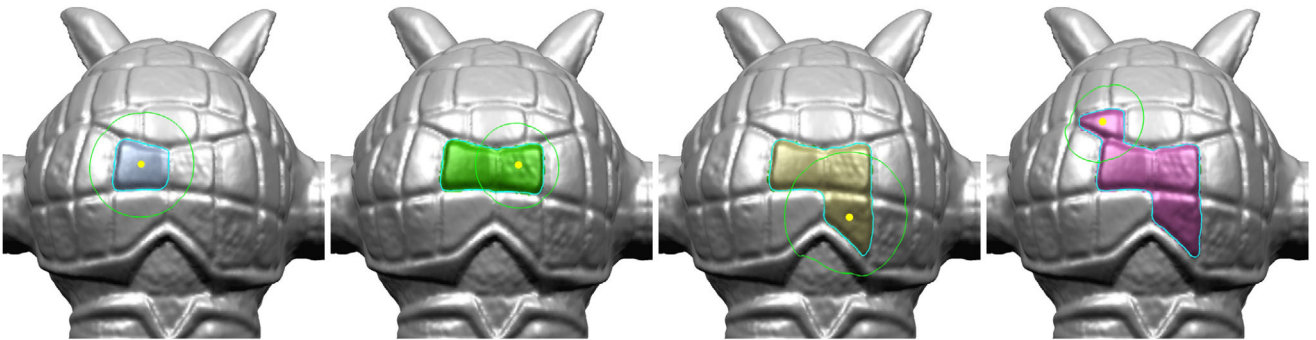


Figure 17: Sequence of additive segmentations.

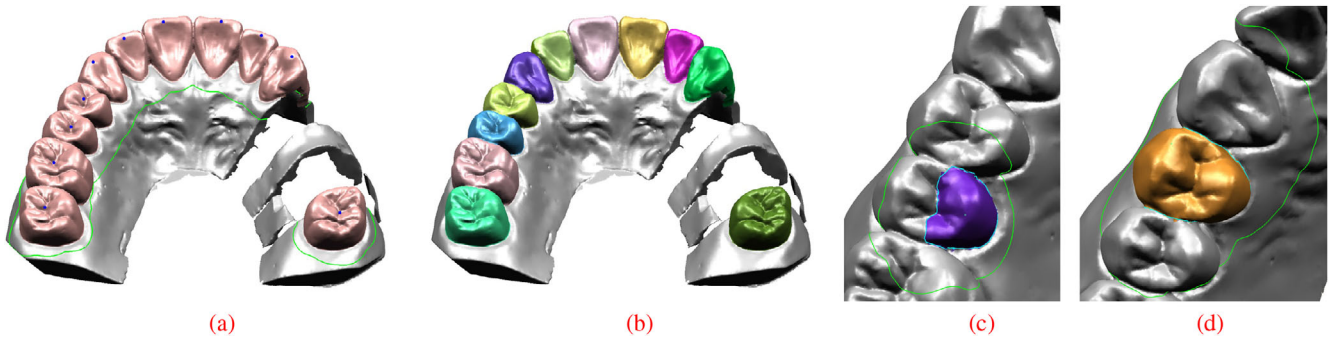


Figure 18: Segmentation of 3D scanned tooth model.

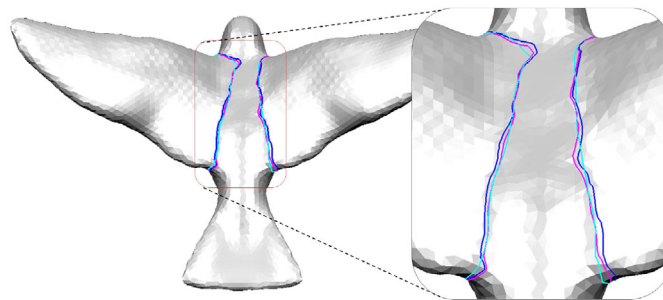


Figure 19: Comparison of three segmentation boundaries: dot scissor (in blue), initial isoline (in magenta) and anisotropic geodesics (in cyan).

Table 1: Comparison of several segmentation boundaries.

Segmentation boundary	(a) Sum of mean curvature	(b) Length	(a)/(b)
Initial isoline	10.695432	1.328787	8.049017
Left wing	Aniso. geodesic	10.930929	8.865425
	Dot scissor	9.656585	7.658317
Right wing	Initial isoline	11.522935	7.711203
	Aniso. geodesic	10.197441	8.085232
	Dot scissor	10.288594	1.329011

(in magenta) and anisotropic geodesics (in cyan). Based on the minima rule [HR84, HS97], we evaluated the segmentation boundary by measuring the mean curvature per unit length. More specifically, we computed the sum of the mean curvatures at the edge intersections with each segmentation boundary and divided it by its length. The evaluation results of the segmentation boundaries in Figure 19 are listed in Table 1, wherein the geodesic segmentation boundary shows a higher mean curvature per unit length.

Note that we employed a mean curvature for an unbiased comparison; because the dot scissor and the proposed method generally generated different harmonic fields. Figure 20 compares various segmentation boundaries generated by dot scissor and our method, respectively.

We performed quantitative evaluations of our segmentation results using the PSB dataset, which includes 380 models from 19 object categories. We randomly chose 19 models—one for each category—and requested several users to segment each model into parts without giving any specific information about the number of parts. Figure 21 shows the results of the mesh segmentations obtained by a user. Each feature region was segmented by a single mouse click on the candidate region of an appropriate radius controlled by the user. On an average, it took less than 1 min for the simple models and less than 2 min for the complex models with several parts. Based on the protocols in Chen *et al.* [CGF09], we measured four error metrics: *Cut Discrepancy (CD)*; *Hamming Distance (HD)*; *Rand Index (RI)*; and *Consistency Error (CE)*. We referred to these protocols for more details on the error metrics. Figure 22 shows the evaluation results by comparing

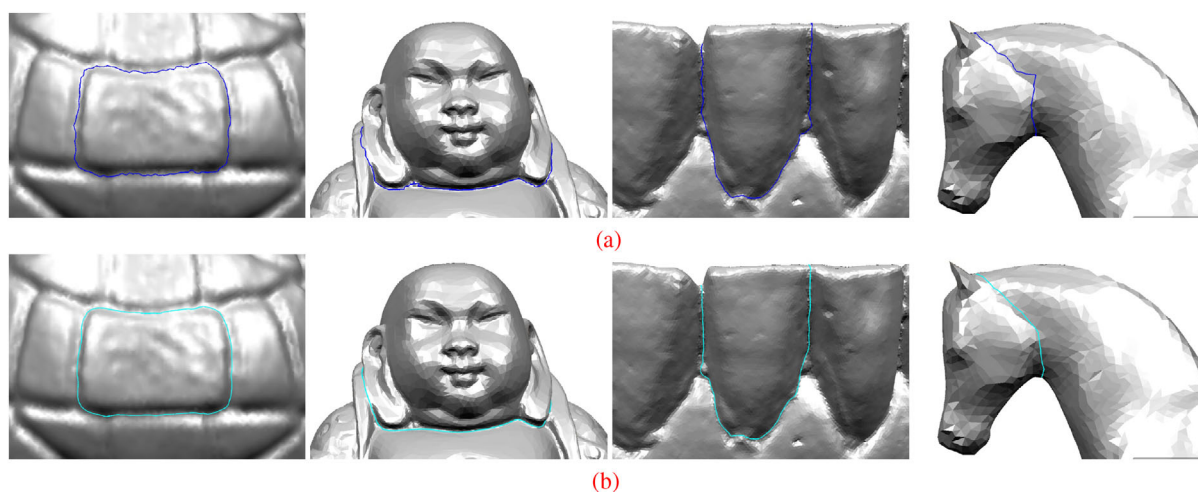


Figure 20: Comparison of segmentation boundaries generated by (a) dot scissor (in blue) and (b) ROI scissor (in cyan). ROI, region of interest.



Figure 21: Mesh segmentation results using PSB data set [CGF09]. PSB, Princeton Segmentation Benchmark.

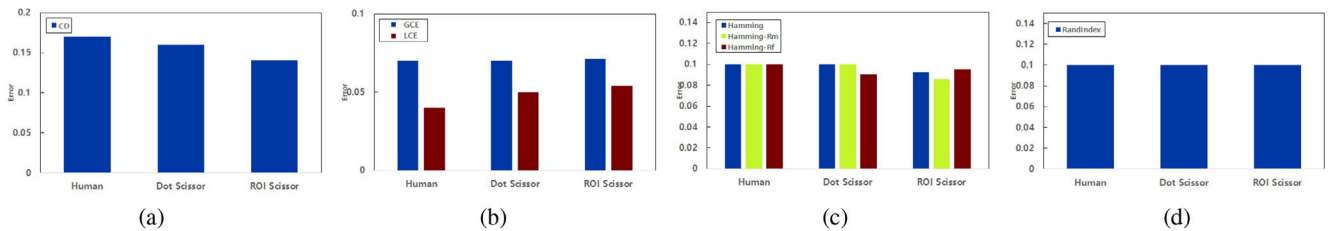


Figure 22: Evaluation of segmentation results using the protocols in Chen et al. [CGF09]: (a) CD, (b) CE, (c) HD and (d) RI. CD, Cut Discrepancy; CE, Consistency Error; HD, Hamming Distance; RI, Rand Index.

our method with manual segmentation and the dot scissor, respectively. Our results showed lower or similar errors than those of these methods.

The proposed method showed interactive speed for all the examples tested in the experimental results (see supplemental video). Computation time consists of three components: (i) construction

of the harmonic field; (ii) selection of the initial isoline and feature points and (iii) construction of the anisotropic geodesics. Since the computations are restricted to the candidate region, the computation time is proportional to the number of vertices or faces in the candidate region. Table 2 shows the detailed results of the computation times for some segmentation results in Figure 21.

Table 2: Timing results for the segmentations of models in Figure 21.

Name(part)	Model		Time (in ms)			
	#Vertex of candidate region	#Face of candidate region	Concavity-aware harmonic field	Initial segmentation boundary and selection of feature points	Anisotropic geodesic boundary	Total
Bearing(upper)	1272	2441	8.8334	22.4485	0.95475	32.2366
Plier(handle)	2297	4514	10.4446	3.9224	0.6058	14.9728
Dolphin(tail)	1330	2611	5.4067	4.6563	0.7861	10.8491
Chair(leg)	1165	2269	5.572	6.6053	0.5983	12.7756
Bird(wing)	3940	7724	17.0493	5.9612	0.8089	23.8194
Horse(neck)	1238	2405	8.8606	7.2564	0.5969	16.7139
Airplane(wing)	1969	3870	11.0634	8.5171	0.878	20.4585
Octopus(head)	3338	6566	18.798	5.4619	1.9461	26.2060
Hand(index)	3541	6865	13.734	6.4676	0.5102	20.7118
Glasses(frame)	2149	4220	10.4589	6.8879	0.5509	17.8977
Giraffe(neck)	5014	9869	21.4279	9.7341	0.8896	32.0516
human(arm)	7291	14,354	27.8941	17.9009	0.8233	46.6138
Vase(handle)	6379	12,534	25.4951	20.4722	1.299	47.2663
Cup(handle)	5490	10,815	26.011	20.8542	1.3618	48.2270
Armadillo(arm)	10,442	20,569	53.5425	60.004	0.5611	114.1076

6. Conclusion

We proposed a simple and effective interface, the *ROI scissor*, for the interactive segmentation of feature regions in a triangular mesh. Our method is based on a concavity-aware harmonic field and anisotropic geodesics. The concavity-aware harmonic field is improved by our sophisticated weighting scheme, allowing it to identify concave regions more clearly. Also anisotropic geodesics can be automatically constructed by providing feature points carefully selected from the improved harmonic field. In the experimental results, we demonstrated the usability, controllability and consistency of the proposed method through several segmentation results for various 3D models, including the PSB dataset [CGF09]. Based on a quantitative evaluation, our method showed slightly lower or similar errors compared to those of manual segmentations and existing methods.

In the current implementation, segmentation results can be affected by the candidate region and its manual control can be a weakness of the proposed method even though an effective control mechanism is provided. Once the radius of a candidate region is determined, it remains unchanged until a new one is set. Therefore, the user does not need to adjust the candidate region as long as the desired feature region is contained in the candidate region. However, it would be necessary to increase the radius of candidate region whenever the desired feature region is not inside the current candidate region. Figure 18c shows an example of such case where the candidate region (in green) is too small to cover the desired tooth. In this case, the user has two options: (i) expanding the candidate region, or (ii) performing additive segmentation explained above. Large candidate region has a relatively small effect on the segmentation result if the desired feature region has a definite concave boundary as shown in Figure 18d. Even if there exist several candidate boundaries, our method will find the best one with maximum variation of a harmonic field.

In future research, we plan to extend the proposed method to automatic segmentation for a specific type of models. For this, we need to find how to determine the radius of the candidate region and click position automatically. We also plan to develop a segmentation method for volumetric meshes. Since it is difficult to construct a segmentation field on a volumetric mesh, further research will be necessary.

Acknowledgements

We would like to thank our anonymous reviewers for their comments. This work was supported by the National Research Foundation of Korea (NRF) grant funded by the Korea government (MSIT) (NRF-2019K1A3A1A78112596, NRF-2020R1F1A1048472, NRF-2021R1A2C2012663).

References

- [AZC*11] AU O. K.-C., ZHENG Y., CHEN M., XU P., TAI C.-L.: Mesh segmentation with concavity-aware fields. *IEEE Transactions on Visualization and Computer Graphics* 18, 7 (2011), 1125–1134.
- [BKP*10] BOTSCH M., KOBELT L., PAULY M., ALLIEZ P., LÉVY B.: *Polygon Mesh Processing*. A K Peters, Natick, Massachusetts, 2010.
- [CBK12] CAMPEN M., BOMMES D., KOBELT L.: Dual loops meshing: Quality quad layouts on manifolds. *ACM Transaction on Graphics* 31, 4 (2012), 1–11.

- [CDST97] CHAZELLE B., DOBKIN D. P., SHOURABOURA N., TAL A.: Strategies for polyhedral surface decomposition: An experimental study. *Computational Geometry* 7, 5-6 (1997), 327–342.
- [CGF09] CHEN X., GOLOVINSKIY A., FUNKHOUSER T.: A benchmark for 3D mesh segmentation. *ACM Transactions on Graphics (TOG)* 28, 3 (2009), 1–12.
- [CH90] CHEN J., HAN Y.: Shortest paths on a polyhedron. In *Proceedings of the 6th Annual Symposium on Computational Geometry* (1990), pp. 360–369.
- [CHK13] CAMPEN M., HEISTERMANN M., KOBELT L.: Practical anisotropic geodesy. *Computer Graphics Forum* 32, 5 (2013), 63–71.
- [HR84] HOFFMAN D. D., RICHARDS W. A.: Parts of recognition. *Cognition* 18, 1-3 (1984), 65–96.
- [HS97] HOFFMAN D. D., SINGH M.: Saliency of visual parts. *Cognition* 63, 1 (1997), 29–78.
- [JLCW06] JI Z., LIU L., CHEN Z., WANG G.: Easy mesh cutting. *Computer Graphics Forum* 25, 3 (2006), 283–291.
- [KMZ10] KOVACS D., MYLES A., ZORIN D.: Anisotropic quadrangulation. In *Proceedings of the 14th ACM Symposium on Solid and Physical Modeling* (2010), Association for Computing Machinery, pp. 137–146.
- [KT03] KATZ S., TAL A.: Hierarchical mesh decomposition using fuzzy clustering and cuts. *ACM Transactions on Graphics (TOG)* 22, 3 (2003), 954–961.
- [LDB17] LUCQUIN V., DEGUY S., BOUBEKEUR T.: SeamCut: Interactive mesh segmentation for parameterization. In *SIGGRAPH Asia 2017 Technical Briefs* (2017), pp. 1–4.
- [LLZ*15] LIAO S.-h., LIU S.-j., ZOU B.-j., DING X., LIANG Y., HUANG J.-h.: Automatic tooth segmentation of dental mesh based on harmonic fields. *BioMed Research International 2015* (2015), 1–10.
- [MDSB03] MEYER M., DESBRUN M., SCHRÖDER P., BARR A. H.: Discrete differential-geometry operators for triangulated 2-manifolds. In *Visualization and Mathematics III*. Springer, Berlin, Heidelberg (2003), pp. 35–57.
- [MFL11] MENG M., FAN L., LIU L.: iCutter: A direct cut-out tool for 3d shapes. *Computer Animation & Virtual Worlds* 22, 4 (2011), 335–342.
- [MMP87] MITCHELL J. S., MOUNT D. M., PAPADIMITRIOU C. H.: The discrete geodesic problem. *SIAM Journal on Computing* 16, 4 (1987), 647–668.
- [MW98] MANGAN A. P., WHITAKER R. T.: Surface segmentation using morphological watersheds. In *Proceedings of the IEEE Visualization* (1998).
- [MW99] MANGAN A. P., WHITAKER R. T.: Partitioning 3D surface meshes using watershed segmentation. *IEEE Transactions on Visualization and Computer Graphics* 5, 4 (1999), 308–321.
- [PSH*04] POTTMANN H., STEINER T., HOFER M., HAIDER C., HANBURY A.: The isophotic metric and its application to feature sensitive morphology on surfaces. In *Proceedings of the 8th European Conference on Computer Vision (ECCV)* (2004), pp. 560–572.
- [RMG18] RODRIGUES R. S., MORGADO J. F., GOMES A. J.: Part-based mesh segmentation: A survey. *Computer Graphics Forum* 37, 6 (2018), 235–274.
- [Ser83] SERRA J.: *Image Analysis and Mathematical Morphology*. Academic Press, Inc., London, 1983.
- [SSK*05] SURAZHISKY V., SURAZHISKY T., KIRSANOV D., GORTLER S. J., HOPPE H.: Fast exact and approximate geodesics on meshes. *ACM Transactions on Graphics (TOG)* 24, 3 (2005), 553–560.
- [XLZ18] XU X., LIU C., ZHENG Y.: 3D tooth segmentation and labeling using deep convolutional neural networks. *IEEE Transactions on Visualization and Computer Graphics* 25, 7 (2018), 2336–2348.
- [XW09] XIN S.-Q., WANG G.-J.: Improving Chen and Han’s algorithm on the discrete geodesic problem. *ACM Transactions on Graphics (TOG)* 28, 4 (2009), 1–8.
- [YWZK20] YANG S., WANG R., ZHAO W., KE Y.: 3D intelligent scissors for dental mesh segmentation. *Computational and Mathematical Methods in Medicine 2020* (2020), 1394231.
- [ZLL*15] ZOU B.-j., LIU S.-j., LIAO S.-h., DING X., LIANG Y.: Interactive tooth partition of dental mesh base on tooth-target harmonic field. *Computers in Biology and Medicine* 56 (2015), 132–144.
- [ZLS*20] ZHANG J., LI C., SONG Q., GAO L., LAI Y.-K.: Automatic 3D tooth segmentation using convolutional neural networks in harmonic parameter space. *Graphical Models* 109 (2020), 101071.
- [ZT10] ZHENG Y., TAI C.-L.: Mesh decomposition with cross-boundary brushes. *Computer Graphics Forum* 29, 2 (2010), 527–535.
- [ZTA11] ZHENG Y., TAI C.-L., AU O. K.-C.: Dot scissor: A single-click interface for mesh segmentation. *IEEE Transactions on Visualization and Computer Graphics* 18, 8 (2011), 1304–1312.
- [ZZCJ14] ZHUANG Y., ZOU M., CARR N., JU T.: Anisotropic geodesics for live-wire mesh segmentation. *Computer Graphics Forum* 33, 7 (2014), 111–120.

Supporting Information

Additional supporting information may be found online in the Supporting Information section at the end of the article.

Supporting Information